# Along-slope current generation by obliquely incident internal waves

By OLEG ZIKANOV and DONALD N. SLINN

Department of Ocean Engineering, Florida Atlantic University, Boca Raton, FL 33431-0991, USA

A series of numerical experiments is performed to investigate the breaking of obliquely incident internal waves propagating towards a bottom slope. The case of critical reflection is considered, where the angle between the wave group velocity vector and the horizontal matches the bottom slope angle. The flow evolution is found to be significantly different from the evolution observed previously in simulations of normally incident waves. The divergence of the Reynolds stress in the breaking zone causes a strong along-slope mean current, which changes the flow structure dramatically. The wave does not penetrate the current but breaks down at its upper surface as the result of a critical layer interaction. A continuously broadening mean along-slope current with an approximately constant velocity is produced. We propose a simple model of the process based on the momentum conservation law and the radiation stress concept. The model predictions are verified against the numerical results and are used to evaluate the possible strength of along-slope currents generated by this process in the ocean.

## 1. Introduction

Understanding the mechanism of diapycnal (vertical) mixing in the ocean has been a long-time challenge for physical oceanography. In nature, vertical mixing is inhibited by the ocean's stable stratification. Munk (1966) showed that a basin-averaged vertical eddy diffusivity of roughly $\kappa = 10^{-4} \, \mathrm{m^2 \, s^{-1}}$ must exist to balance the effects of upwelling and downward diffusion. Field studies, however, have failed to observe such large vertical diffusivities in the ocean interior, falling short by approximately an order of magnitude (see e.g. Ledwell, Watson & Law 1993 and Polzin *et al.* 1997). The conclusion from the field experiments is that 80–90% of the vertical mixing is not taking place in the ocean interior. Instead, the mixing is expected to occur near boundaries.

Field experiments by Eriksen (1985, 1998) have suggested that the oceanic internal wave field can provide sufficient energy to activate strong mixing near sloping boundaries, which can in turn account for a significant portion of the overall oceanic vertical mixing. One mechanism by which this may occur is the breaking of internal gravity waves, as they reflect off the continental shelf or other sloping boundaries near islands or seamounts. When an internal wave of frequency $\omega$ propagating in a uniformly stratified environment reflects from a larger-scale, sloping boundary, its angle of propagation with respect to the horizontal is preserved (Phillips 1977). The wave frequency, $\omega$, depends on the inclination, $\theta$, of the wavenumber vector to the horizontal and the background density stratification according to the

dispersion relation

$$\omega = N \cos\theta, \tag{1}$$

where $N$ is the buoyancy frequency defined by

$$N \equiv \left( -\frac{g}{\rho_0} \frac{\partial \bar{\rho}}{\partial z} \right)^{1/2}, \tag{2}$$

$\partial \bar{\rho}(z)/\partial z$ and $\rho_0$ being the background density gradient and the reference density.

The reflection from a sloping boundary can lead to an increase in the energy density of the wave, as the energy in the oncoming wave is concentrated into a more narrow ray tube upon reflection. The situation probably most effective for boundary mixing arises when an oncoming wave reflects from a bottom slope $\alpha$ that nearly matches the angle of wave propagation $\pi/2 - \theta$. In this case linear theory suggests that a small-amplitude oncoming wave may be reflected with large amplitude, thus exhibiting nonlinear behaviour and possibly wave breaking and turbulence. The flux of reflected energy is transferred to shorter wavelength and the group velocity decreases. At the critical condition, $\pi/2 - \theta = \alpha$, linear wave theory predicts a reflected wave of infinite amplitude, infinitesimal wavelength, and zero group velocity, leading to the trapping of oncoming wave energy in the boundary region. In such a case, nonlinearities and turbulence come into play. This phenomenon was considered in laboratory experiments by Cacchione & Wunsch (1974), Ivey & Nokes (1989), and De Silva, Imberger & Ivey (1997).

The nonlinear dynamics of the reflection of an internal wave propagating at the critical angle was the subject of extensive numerical experiments by Slinn & Riley (1996, 1998*a, b*, 2001). A wave train of stationary amplitude was generated in such a way that the wave approached the bottom in the normal plane. The numerical simulations provided firm evidence that the wave breaking near the boundary can generate intensive turbulent motions. The flow was found to depend on the bottom slope. In the case of steep slope ($\sim 30°$), it developed a quasi-steady turbulent bore moving upslope at the phase speed of the wave. For shallow slopes ($\sim 5°$), which are much more common in the ocean, the wave breakdown led to an intermittently turbulent boundary flow with the time period of about 1.3 wave periods. The energy of the oncoming wave was distributed in an approximately constant proportion so that about 35% went into irreversible mixing, 55% was dissipated to heat, and 10% reflected from the bottom.

The numerical simulations by Slinn & Riley concerned an idealized situation in the sense that only normally incident waves were considered. Field observations, of course, contain waves that approach the slope from a full spectrum of incident angles. In this paper, we shall consider oblique waves and find drastic changes in the flow structure.

The first concept we need to invoke here is that of an along-slope current generated by an obliquely oncoming wave. We use the terminology 'along-slope' to mean a velocity component along the slope, as opposed to an up-slope or down-slope current (see figure 1 for an illustration). Aspects of the generation of a mean current by obliquely incident internal waves have been predicted by Hogg (1971), Wunsh (1973) and Thorpe (1997, 1999), based on different physical mechanisms. Wunsh (1973) explained the slow surface drift observed in large lakes by the Lagrange drift generated by a second-order interaction of internal waves. Second-order effects were also considered by Thorpe (1997). It was shown that a resonant interaction of an obliquely incident internal wave with its reflected counterpart can generate a Stokes drift in the along-slope direction.
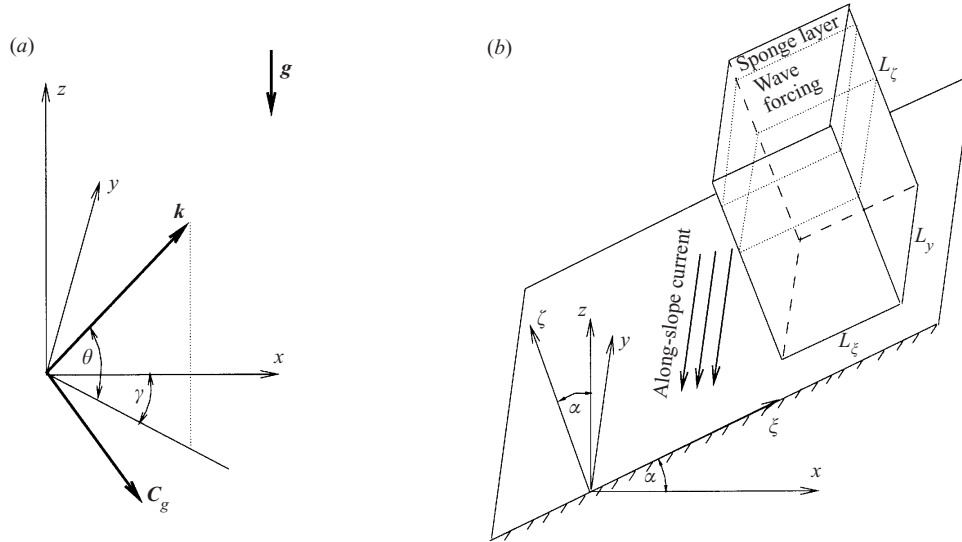
FIGURE 1. Model geometry: (*a*) wavenumber vector (*k*) and group velocity (*C*$_g$) of the wave; (*b*) the bottom slope, computational domain, and the coordinate systems used in the simulations. $\theta$ and $\gamma$ are the inclination and oblique angles; $\alpha$ is the slope angle; $\xi$-axis is up-slope and $y$-axis is in the along-slope direction.

In the studies by Hogg (1971) and Thorpe (1999), the along-slope current generation was attributed to the divergence of the Reynolds stress caused by wave breakdown in increasingly shallow water (Hogg) or by imperfect viscous reflection at the bottom slope (Thorpe). An analogous process occurs for surface wave breaking at the shore when waves approach the beach at an oblique angle. An along-shore current (see Slinn *et al.* 1998; Slinn, Allen & Holman 2000) can develop in the surf zone from the flux of surface wave momentum. This process has also been explained using the concept of radiation stress (Bowen 1969; Longuet-Higgins 1970). Simply stated, if a reflected wave train does not carry as much momentum away from a boundary as is carried toward the boundary by an incident wave train, then there will be a compensating flux of momentum into a mean flow.

An experimental verification of the possibility of current generation by internal gravity waves approaching a sloping boundary at an oblique angle can be found in Dunkerton, Delisi & Lelong (1998). Despite limitations imposed by the size of the experimental tank, generation of along-slope currents was clearly observed.

A second well-established concept important for our analysis is that of the instability and breakdown of an internal wave near a critical layer. The notion of a critical layer refers to an internal wave propagating through an ambient shear flow. Consider the situation when the mean flow velocity $U(z)$ grows with the transverse coordinate $z$ and the wave has a non-zero $z$-component of the group velocity so it propagates across the mean current. The critical layer can be defined as a layer $z = z_c$ at which the growing $U(z)$ becomes equal to the component $\omega/k_i$ of the trace speed in the direction parallel to the mean flow so that the intrinsic frequency $\omega - k_i U$ tends toward zero.

Inviscid studies using the WKB approximation (Bretherton 1966) and the linear approximation (Booker & Bretherton 1967) revealed that only a small part (dependent on the local Richardson number) of the wave energy penetrates the critical layer.

A much larger part is absorbed by the ambient current. The asymptotic (WKB and linear) studies failed to describe the singular behaviour of the internal wave approaching the critical level. They pointed out, however, unambiguously that, as the $z$-component of the group velocity and the wavelength tend to zero with $z \to z_c$, and the energy density of the wave packet grows as $(z - z_c)^{-1}$, the wave becomes unstable and should break in a turbulent manner. It should be stressed that, according to this scenario, the wave breakdown can occur before the actual critical layer condition is fulfilled provided the mean flow velocity grows to close to the trace speed and the wave energy is large enough.

Since then, the transfer of the internal wave energy into small-scale turbulence during the critical level interactions has been held responsible for a considerable part of the turbulent mixing in the ocean interior. Internal wave breaking was studied using laboratory experiments (Thorpe 1981; Koop 1981; Koop & McGee 1986) and numerical analysis (Winters & Riley 1992; Winters & D'Asaro 1994). (We mentioned only the three-dimensional numerical simulations because of the decisive importance of three-dimensionality for a correct description of the wave breaking process demonstrated in these studies.) The case of a wave propagating normally to the mean current was considered. It was found that approximately one third of the wave energy went into the increase of the kinetic energy of the mean flow, one third was reflected, and one third was dissipated in the turbulent flow developing at the critical layer.

Combining the ideas of along-slope current generation by an obliquely incident internal wave and wave breaking at the critical layer, it is straightforward to assume the possibility of the following hypothetical scenario. Consider an internal wave propagating towards the bottom slope over a long period of time and assume that the propagation is at the critical angle, $\pi/2 - \theta = \alpha$. Since no reflection occurs in this case, the linear momentum continuously transferred by the wave is trapped in the boundary region. This leads to the generation and growth of an along-slope current. As soon as the magnitude of the current velocity approaches the trace speed in the along-slope direction, wave breaking at a critical layer replaces the bottom breaking. It does not change the fact that a part of the wave linear momentum is transferred to the mean current. A consequence is the growth in the current strength and moving of the wave breaking layer away from the bottom. In such a manner the along-slope flow increases as long as the oncoming wave continues to support it with its momentum flux.

The numerical experiments presented in this paper confirm that this scenario is, indeed, realistic. After discussing the formulation of the problem and numerical method in §2 we propose a simple theoretical model of the process in §3. The results of the numerical experiments are presented in §4. In §5, we evaluate the possibility of mean current generation in real oceanic flows. Concluding remarks and general discussion are given in §6.

## 2. Numerical model

In this section, we give a brief account of the model used in the computations. More details can be found in Slinn & Riley (1998b).

### 2.1. *Governing equations*

We adopt the Boussinesq approximation for flows of stratified fluid. In a coordinate system with the $z$-axis in the vertical direction, the dimensionless equations of fluid

motion are

$$\nabla \cdot \boldsymbol{u} = 0, \tag{3}$$

$$\frac{\partial \boldsymbol{u}}{\partial t} + (\boldsymbol{u} \cdot \nabla)\boldsymbol{u} = -\nabla p - Ri\, \boldsymbol{e}_z \rho + \frac{1}{Re}\nabla^2 \boldsymbol{u} + \boldsymbol{F_u}, \tag{4}$$

$$\frac{\partial \rho}{\partial t} + \boldsymbol{u} \cdot \nabla \rho - \boldsymbol{u} \cdot \boldsymbol{e}_z = \frac{1}{Pe}\nabla^2 \rho + F_\rho. \tag{5}$$

Here $\boldsymbol{u}$ is the velocity field, $\rho$ and $p$ are the perturbations of the density and pressure fields, $\boldsymbol{e}_z$ is the unit vector in the direction opposing gravity, and $\boldsymbol{F_u}$, $F_\rho$ are the forcing terms discussed below. The background density and pressure distributions are

$$\tilde{\rho}_0 + \frac{\mathrm{d}\bar{\rho}}{\mathrm{d}z}z \quad \text{and} \quad \tilde{p}_0 - \tilde{\rho}_0 gz, \tag{6}$$

where the vertical gradient $\mathrm{d}\bar{\rho}/\mathrm{d}z$ due to the gradients of salinity and temperature is assumed to be constant and the dimensional reference density field $\tilde{\rho}_0$ is in hydrostatic balance with the mean pressure gradient.

The equations (3)–(5) are non-dimensionalized using the parameters of the incident wave and background stratification as scales. In particular, we use the wavelength $\lambda_\zeta$ in the direction normal to the slope as the length scale and $\lambda_\zeta|\mathrm{d}\bar{\rho}/\mathrm{d}z|$ as the density scale. The non-dimensional total density field is then expressed as

$$\rho_t = \rho_0 - z + \rho(x, y, z, t). \tag{7}$$

A peculiarity of our formulation is that the natural choice for the velocity scale, the amplitude $A$ of the velocity oscillations in the wave, depends on the details of forcing in a complex fashion and cannot be reliably determined prior to the simulations. Therefore, we apply an arbitrary chosen velocity scale $U = 0.1\,\mathrm{m\,s^{-1}}$ and the corresponding time scale $\lambda_\zeta/U$ in every numerical run.

The non-dimensional parameters are the Reynolds, Richardson, and Péclet numbers defined according to

$$Re \equiv \frac{U\lambda_\zeta}{\nu}, \quad Ri \equiv \left(\frac{N\lambda_\zeta}{U}\right)^2, \quad Pe \equiv \frac{U\lambda_\zeta}{\kappa}, \tag{8}$$

where $\nu$ and $\kappa$ are the kinematic viscosity and the diffusivity of density fluctuations, and $N$ is the buoyancy frequency defined by (2). The 'real' parameters (8) are evaluated after the calculations using the computed value of the wave amplitude $A$ instead of $U$.

Typically for ocean water, $\kappa$ is several orders of magnitude smaller than $\nu$. In turbulent flows, however, both density and momentum diffusion are dominated by transport due to small-scale velocity fluctuations, which are subject to the subgrid-scale modelling in our calculations. Therefore, we follow the approach commonly used in simulation of turbulent convection and scalar transfer and assume that $Pe = Re$.

### 2.2. *Model geometry and forcing*

The geometry of the model is illustrated in figure 1. The orientation of the oncoming wave is determined using the inclination $\theta$ of the wavenumber vector $\boldsymbol{k}$ to the horizontal and the oblique angle $\gamma$ (see figure 1*a*).

In non-dimensional variables, the components of the trace speed are defined according to

$$C_x^{tr} \equiv \frac{\omega}{k_x}, \quad C_y^{tr} \equiv \frac{\omega}{k_y}, \quad C_z^{tr} \equiv \frac{\omega}{k_z}, \tag{9}$$

where $\omega$ is the wave frequency determined through the non-dimensional form of the dispersion relation (1)

$$\omega^2 = Ri \frac{k_x^2 + k_y^2}{k^2}.$$

Sometimes (see e.g. Thorpe 1997, 1999 or Winters & D'Asaro 1994) expressions (9) are called phase speed or phase velocity of the wave. We prefer the name 'trace speed' to distinguish (9) from the real phase velocity vector (see Phillips 1977)

$$\boldsymbol{C}_{ph} \equiv \left| \frac{\omega}{k} \right| \frac{\boldsymbol{k}}{k}. \tag{10}$$

The group velocity vector defined as

$$\boldsymbol{C}_g \equiv \nabla_k \omega(\boldsymbol{k}) \tag{11}$$

is normal to $\boldsymbol{k}$ (Phillips 1977).

It is advantageous to perform the calculations in the coordinate system rotated about the along-slope $y$-axis by the angle of the slope $\alpha$. The rotated system $(\xi, y, \zeta)$ has the $\xi$-axis directed up-slope and the $\zeta$-axis perpendicular to the slope (figure 1$b$). The most important advantage is that we can use a rectangular computational domain and apply the periodic boundary conditions in the $\xi$- and $y$-directions. Note that the background density and pressure fields (6), which are inhomogeneous in the $\zeta$-direction, are subtracted from the total fields in the equations (3)–(5).

The oncoming wave is continuously generated from inside the computational domain utilizing spatially localized forcing terms. The two-dimensional forcing method of Slinn & Riley (1998$b$) has been generalized by P. N. Lombard & J. J. Riley (1998, private communication) to include the three-dimensional case of oblique wave incidence. In the rotated coordinate system

$$\left.\begin{aligned}
F_u &= \frac{C}{k_\xi^2 c - k_\zeta k_\xi s + k_y^2 c} \\
&\qquad [F(\zeta)(k_y^2 s - k_\xi k_\zeta c + k_\zeta^2 s)\cos\Phi - F'(\zeta)(k_\xi c - k_\zeta s)\sin\Phi], \\
F_v &= -\frac{C}{k_\xi^2 c - k_\zeta k_\xi s + k_y^2 c}[F(\zeta)(k_\zeta k_y c + k_\xi k_y s)\cos\Phi + F'(\zeta)k_y c \sin\Phi], \\
F_w &= CF(\zeta)\cos\Phi, \\
F_\rho &= -\frac{C[(k_\xi c - k_\zeta s)^2 + k_y^2]}{\omega(k_\xi^2 c - k_\zeta k_\xi s + k_y^2 c)}[F(\zeta)\sin\phi + F'(\zeta)s(k_\xi c - k_\zeta s)\cos\varphi].
\end{aligned}\right\} \tag{12}$$

Here $c$ and $s$ stand for $\cos\alpha$ and $\sin\alpha$, respectively, $C$ is the forcing amplitude, $\boldsymbol{k} = (k_\xi, k_y, k_\zeta)$ is the wavenumber vector, $\boldsymbol{u} = (u, v, w)$ is the velocity in $(\xi, y, \zeta)$ directions, $\Phi = k_\xi \xi + k_y y + k_\zeta \zeta + \omega t$ is the phase of the wave, and

$$\omega^2 = Ri \frac{(k_\xi c - k_\zeta s)^2 + k_y^2}{k_\xi^2 + k_y^2 + k_\zeta^2}.$$

The forcing localization function is

$$F(\zeta) = \exp[-b(\zeta - \zeta_f)^2], \quad 0 \leqslant \zeta \leqslant L_\zeta,$$

where $L_\zeta$ is the height of the computational domain. $F'(\zeta)$ is the $\zeta$-derivative of $F(\zeta)$. The parameters $\zeta_f$ and $b$ are chosen in such a way as to localize the forcing region in
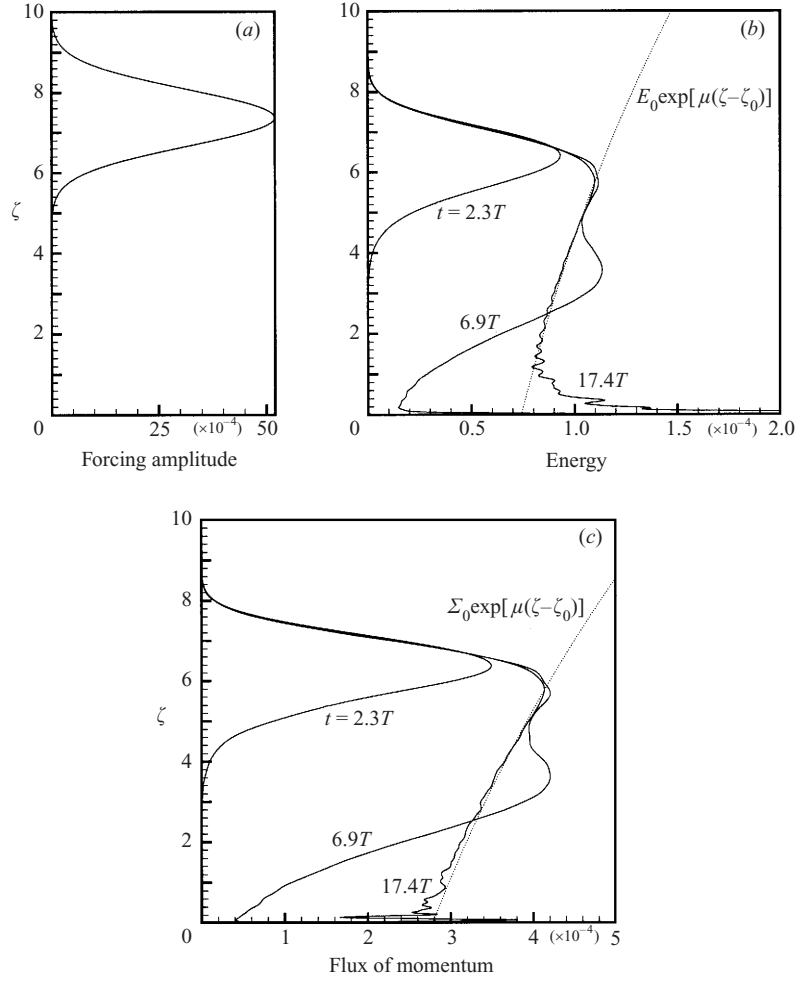
FIGURE 2. (a) Forcing localization function $F(\zeta)$; (b) and (c) calculations for Case 1 (see §4). $\xi, y$-averaged total energy $E(\zeta, t) = (1/2)\langle u^2 + v^2 + w^2 + Ri\rho^2 \rangle$ and flux of $y$-momentum in the negative $\zeta$-direction $\Sigma(\zeta, t) = -\langle wv \rangle$ are shown as functions of $\zeta$ at different $t$. Dotted lines are the exact solutions for viscous decay of a monochromatic wave, $\mu = -2k^2 Re^{-1} C_{g\zeta}^{-1}$.

the upper half of the domain and having the width exceeding the wavelength in the $\zeta$-direction, $\lambda_\zeta$ (cf. figure 2a). It was shown by Slinn & Riley (1998b) and confirmed by our calculations that the forcing produces a nearly monochromatic, time-uniform wave.

### 2.3. *Boundary conditions*

The boundary conditions on the lateral boundaries of the computational domain are those of periodicity in the $\xi$- and $y$-directions. At the bottom, a no-slip condition on the velocity is applied. For the density field, we employ a zero-flux boundary condition

$$\left. \frac{\partial \rho_t}{\partial \zeta} \right|_{\zeta=0} = 0.$$

Substituting the expression (7) for the total density we obtain

$$\frac{\partial \rho}{\partial \zeta}\bigg|_{\zeta=0} = \cos \alpha. \tag{13}$$

The flow above the forcing region is of minimal interest in the present study. The only problem to is wave reflection from the upper boundary, which could contaminate the computed results. Following Slinn & Riley (1998*b*) we apply the Rayleigh damping sponge layer (Durran *et al.* 1993) at the top of the computational domain. This layer occupies the upper 13 grid points ($\sim 0.8\lambda_\zeta$ in height) and absorbs the energy of upward propagating waves with minimum reflection.

### 2.4. *Numerical method and subgrid-scale filtering*

The numerical method is reported in full detail by Slinn & Riley (1998*b*). Only a cursory description is given here. We employ the fourth-order compact Padé scheme for spatial discretization and the third-order Adams–Bashforth time-stepping technique. A computational grid of variable density is used, grid points being clustered near the bottom.

Additional artificial numerical dissipation in the form of hyperviscosity terms $\mu\nabla^6 \boldsymbol{u}$, $\mu\nabla^6\rho$ is included into the model. The numerical approximation of these terms is based on the compact filtering technique proposed by Lele (1992). The hyperviscosity filtering is frequently used in the simulation of geophysical flows as a subgrid-scale LES model (see e.g. Lesieur 1987). The process of the internal wave breakdown is not driven by the motions at dissipative scales. Therefore, in our moderate Reynolds number simulations, where the filtered energy is only a small part of the total dissipation (see discussion of figure 9*a* in the Appendix), the presence of the hyperviscous filter does not have a considerable impact on the large-scale properties of the flow.

### 2.5. *Energy balance*

The volume-averaged terms of the energy balance equations are used to analyse the results of the calculations. Following Winters *et al.* (1995) we define the kinetic, potential, and total energies as

$$\overline{KE} \equiv \frac{1}{V}\int_V \frac{1}{2}(u^2 + v^2 + w^2)\mathrm{d}V, \tag{14}$$

$$\overline{PE} \equiv \frac{1}{V}\int_V \frac{1}{2}Ri\,\rho^2\mathrm{d}V, \tag{15}$$

$$\overline{TE} \equiv \overline{KE} + \overline{PE}. \tag{16}$$

The balance equations are

$$\frac{\partial}{\partial t}\overline{KE} = \frac{1}{V}\int_V [B_f + \epsilon + F_{KE} + W_{KE}]\mathrm{d}V$$
$$+ (L_\xi L_y)^{-1}\int_0^{L_\xi}\int_0^{L_y}\left[\tfrac{1}{2}w\,KE + w\,p\right]|_{\zeta=L_\zeta}\mathrm{d}\xi\mathrm{d}y, \tag{17}$$

$$\frac{\partial}{\partial t}\overline{PE} = \frac{1}{V}\int_V [-B_f + \chi + F_{PE} + W_{PE}]\mathrm{d}V$$
$$+ (L_\xi L_y)^{-1}\int_0^{L_\xi}\int_0^{L_y}\left[\tfrac{1}{2}w\,PE\right]|_{\zeta=L_\zeta}\mathrm{d}\xi\mathrm{d}y, \tag{18}$$

where $\epsilon$ and $\chi$ are the rates of dissipation of kinetic and potential energy occurring at the resolved scales, $F_{KE}$ and $F_{PE}$ are the rates of dissipation by the filter, $B_f \equiv Ri\,\rho\,\boldsymbol{u}{\cdot}\boldsymbol{e}_z$ is the buoyancy flux, and $W_{KE}$, $W_{PE}$ are the work input by the forcing mechanism. A negligibly small portion of kinetic energy is also removed in the process of maintaining a zero mean along-slope flow in the forcing region. The surface integral terms in (17) and (18) represent the outward energy flux into the Rayleigh damping sponge layer near the upper boundary of the computational domain. Exact definition of the terms in (17) and (18) and the derivation of the equations can be found in Slinn & Riley (1998*b*).

## 3. Radiation stress model

We postpone the discussion of the numerical experiments until §4 in order to introduce here a simple model for the along-slope current generation. The model will later be used to interpret the results of calculations.

### 3.1. *Radiation stress*

The derivation is based on the conservation of momentum and on the concept of the radiation stress introduced by Longuet-Higgins & Stewart (1964) for surface waves. The notion of the radiation stress is equivalent to the excess flux of momentum created by a propagating wave.

Let us consider a monochromatic internal wave, which is an exact solution to the inviscid, non-diffusive version of (3)–(5) outside the forcing region (Phillips 1977)

$$\left.\begin{aligned}
(u_x, u_y) &= A(v_x, v_y)\sin\theta\cos\Phi,\\
u_z &= -A\cos\theta\cos\Phi,\\
\rho &= A\omega^{-1}\cos\theta\sin\Phi,\\
p &= A|C_{ph}|\tan\theta\cos\Phi.
\end{aligned}\right\} \tag{19}$$

The Cartesian coordinates $(x, y, z)$ (see figure 1*a*) are used in (19); $(u_x, u_y, u_z)$ stand for the velocity components, $\Phi = k_x x + k_y y + k_z z - \omega t$ is the phase of the wave, and $v_x = k_x(k_x^2 + k_y^2)^{-1/2}$ and $v_y = k_y(k_x^2 + k_y^2)^{-1/2}$ are the components of the unit vector parallel to the horizontal projection of the wavenumber vector $\boldsymbol{k} = (k_x, k_y, k_z)$. The wave amplitude and frequency are given by $A$ and $\omega$ and the wave orientation can be defined through the inclination angle $\theta$ and the oblique angle $\gamma = \cos^{-1} v_x = \sin^{-1} v_y$.

The primary interest of our analysis is in the mean flux of momentum towards the bottom slope produced by the wave (19). Therefore, we rewrite the equations of motion (3)–(5) in the rotated coordinate system $(\xi, y, \zeta)$ and take the average in the plane $(\xi, y)$ parallel to the slope. Taking advantage of the flow homogeneity in this plane (periodic boundary conditions applied in §2.3) we obtain the equations for the mean velocity components and density fluctuations. The mean currents in the $\xi$- and $\zeta$-directions are opposed by the vertical gradient of background density and should be weak. For the mean along-slope current, hereafter denoted as $V(\zeta, t)$, we have

$$\frac{\partial}{\partial t} V(\zeta, t) = \frac{\partial}{\partial \zeta} \Sigma(\zeta, t) + \frac{1}{Re} \frac{\partial^2 V}{\partial \zeta^2}, \tag{20}$$

where

$$-\Sigma(\zeta, t) \equiv \langle vw \rangle \tag{21}$$

is the $y, \zeta$-component of the Reynolds stress, $\langle\ \rangle$ standing for the averaging in the

$(\xi, y)$-plane. $\Sigma(\zeta, t)$ is an analogue of the radiation stress used by Longuet-Higgins & Stewart (1964) and Slinn *et al.* (1998, 2000) for the surface waves. It has the obvious physical meaning of the averaged amount of the $y$-component of the momentum transported by the wave in the direction of negative $\zeta$.

In a freely propagating inviscid, non-diffusive wave (19) the momentum flux $\Sigma$ is constant. Transforming the components of the velocity vector into the rotated coordinate system, substituting into (21) and taking the average one obtains

$$\Sigma = \Sigma_0 = \tfrac{1}{2}A^2[\cos\gamma\sin\theta\sin\alpha + \cos\theta\cos\alpha]\sin\gamma\sin\theta. \tag{22}$$

The same formula with a slightly different definition of the wave amplitude $A$ was given by Thorpe (1999). At critical reflection $\theta = \pi/2 - \alpha$, (22) becomes

$$\Sigma_0 = \tfrac{1}{4}A^2\cos\alpha\sin 2\alpha\sin\gamma[\cos\gamma + 1]. \tag{23}$$

If, for some reason, the solution (19) ceases to be correct, $\Sigma$ may become $\zeta$-dependent, which results in generation of the along-slope current $V$ in accordance to (20). Three possible reasons encountered in our simulations are the transient effects near the propagating wave front, decay of the wave due to viscous and diffusive effects, and its breakdown at the bottom or at the critical layer. We consider them in turn.

### 3.2. *Current generation near the wave front and due to viscous and diffusive decay*

In addition to the internal wave breakdown considered in this paper, two mechanisms of the along-slope current generation were encountered in our numerical experiments. They are briefly discussed in this Section. While not having counterparts in the real ocean flows of interest, these mechanisms could contaminate the results of the experiments. Therefore, every precaution was taken to exclude their impact. In particular, the mean along-slope velocity $\langle v \rangle$ was subtracted from the velocity field during the initial, transient phase of each experiment. During the second phase, this procedure was applied in the upper part of the computational domain, while mean currents were allowed to evolve in the lower part, at approximately $\zeta < 0.4L_\zeta$ (see §4.1 for more details).

If not compensated for, strong along-slope currents were found to be generated around the front of the wave propagating in the negative $\zeta$-direction. This happened during the initial phase of the numerical experiments before the wave reached the bottom slope. The obvious explanation is the strong $\zeta$-gradient of the Reynolds stress component $\Sigma$, which has to change, in front of the wave, from zero to a finite value $\Sigma_0$ characteristic of the wave.

A similar mechanism was responsible for wave generation occurring in the forcing region. Here another $\zeta$-gradient of $\Sigma$ exists due to the growth of the wave as it passes through the forcing zone. If left uncompensated this gradient would produce an along-slope current in the direction opposite to the current produced at the wave front.

Even after the wave had reached the bottom slope and a statistically steady incident wave train was established, mean current was generated through the mechanism of viscous decay of the wave. In the presence of viscous dissipation and diffusion, the non-dimensional version of the dispersion relation (1) changes to (Slinn 1995)

$$\omega = \omega_r + i\omega_i,$$

$$\omega_r = Ri^{1/2}\cos\theta - \tfrac{1}{2}k[Pe^{-1} - Re^{-1}]^{1/2}, \tag{24}$$

$$\omega_i = -\tfrac{1}{2}k^2[Pe^{-1} + Re^{-1}]. \tag{25}$$

In the case of $Pe = Re$ considered in this paper, (24) reduces to the inviscid dispersion law (1), while (25) gives the viscous decay of the amplitude of the solution (19) according to

$$A(t) = A(t_0)\exp[-k^2 Re^{-1}(t - t_0)]. \tag{26}$$

We now consider a steady wave train produced by the forcing localized in $\zeta$ but homogeneous in the $\xi$- and $y$-directions. For quantities averaged in $\xi$ and $y$, the time decay (26) can be replaced by the spatial decay

$$A(\zeta) = A(\zeta_0)\exp[-k^2 Re^{-1} C_{g\zeta}^{-1}(\zeta - \zeta_0)]. \tag{27}$$

Here, $C_{g\zeta}$ is the $\zeta$-component of the group velocity. It is negative for a wave propagating toward the bottom. For second-order properties such as kinetic and potential energies or the flux of momentum $\Sigma$ we have

$$\Sigma(\zeta) = \Sigma(\zeta_0)\exp[-2k^2 Re^{-1} C_{g\zeta}^{-1}(\zeta - \zeta_0)]. \tag{28}$$

As discussed in §4, the calculated waves propagate in full agreement with the decay law (28). Moreover, since the calculations are performed at moderate Reynolds number the decay plays an essential part in the solution. In particular, according to (20), the divergence of momentum flux generates a mean current, which can be fairly strong in certain cases. This phenomenon should be considered as unphysical for the simple reason that the Reynolds number for real ocean internal waves is about $10^8$ to $10^9$ (see e.g. Roberts 1975 for field measurement data), which is 5 orders of magnitude larger than in our simulations.

### 3.3. *Current generation due to wave breakdown*

Unlike the viscous decay, the mechanism of current generation discussed in this Section may exist at any Reynolds number and is expected to play an important part in real ocean flows.

Let us assume that the wave breaks in a layer $\zeta_1 \leqslant \zeta \leqslant \zeta_2$ parallel to the bottom. Then the total strength of the along-slope current in this range is increased by the amount $\Sigma(\zeta_2) - \Sigma(\zeta_1)$ minus the amount of momentum carried away by the reflected waves and turbulent vortices generated in the breaking region. In our case of an obliquely incident wave propagating at critical inclination angle, the breaking first occurs when the wave hits the bottom slope. Obviously, this results in the generation of an along-slope current in the boundary region. If the wave flux of momentum (22) is strong enough to compete with the boundary shear stress, the velocity $V$ of the current grows so that it becomes comparable to or even exceeds the along-slope trace speed of the wave,

$$C_y^{tr} = \omega k_y^{-1} = Ri^{1/2}(k_x + k_y)^{1/2}k^{-1}k_y^{-1} = Ri^{1/2}k^{-1}(\sin\gamma)^{-1}, \tag{29}$$

at some distance $\zeta_c$ from the bottom. Then the mechanism of the critical layer instability becomes effective. The wave breaking and, thus, momentum supply into the mean current now occurs in some range around $\zeta_c$. This leads to the growth of $V$ at $\zeta > \zeta_c$ and to the continual shift of the position of $\zeta_c$. As a result, we obtain a progressively broadening zone of the along-slope flow between the bottom and the wave breaking zone.

It should be stressed here that $\zeta_c$ is not necessarily the distance at which the exact critical layer condition is fulfilled. As discussed in the next Section, the wave may break even if the bulk velocity of the mean current is smaller than the trace speed.

For definiteness, $\zeta_c$ will hereafter be considered as an approximate coordinate of the midplane of the wave breaking layer.

We analyse the proposed scenario using the one-dimensional model (20). The viscous decay (28) is neglected so that $\Sigma$ is considered constant outside the breaking zone. We also neglect the fluctuations of $\Sigma(\zeta, t)$ due to the turbulent eddies in the breaking layer. It may be justified by saying that we study the 'slow' evolution on the typical time scale of the growth of the mean current, which is much larger than the typical eddy turnover time.

The boundary conditions are

$$V(0, t) = 0, \quad V(\infty, t) = 0, \quad V(\zeta_c(t), t) = \tau C_y^{tr}, \tag{30}$$

where $\tau$ is an arbitrary coefficient whose presence reflects both the fact that $\zeta_c$ may differ from the exact location of the critical layer and that the wave can break down at a 'sub-critical' value of $V$. This coefficient is presumably close to 1.

Another arbitrary coefficient $0 < \beta < 1$ is used to account for the unknown part of the momentum flux, which is not supplied to the mean current but is carried away by the reflected waves and turbulent vortices. We multiply the wave flux of momentum (22) by $\beta$ and substitute

$$\tilde{\Sigma} = \beta \Sigma \tag{31}$$

into (20). An attempt to estimate $\tau$ and $\beta$ using the results of simulations is made in §4.

Let us consider the situation when, initially, the distance between the critical layer and the bottom grows faster than the thickness of the viscous bottom boundary layer $L(t) = (2Re^{-1}t)^{1/2}$. At some moment of time,

$$\zeta_c(t) \gg L(t)$$

and the viscous term in (20) is negligibly small everywhere but $\zeta < L(t)$. Further, it is assumed that the wave breakdown occurs in a range $\zeta_c - \delta/2 \leqslant \zeta \leqslant \zeta_c + \delta/2$ and that $\delta/2 \ll \zeta_c(t) - L(t)$.

No information is readily available on the details of the wave breaking process, which determines the actual value of $\delta$ and the distribution of $\tilde{\Sigma}(\zeta, t)$ in the wave breaking region. We assume that this process is time-independent on the slow time scale. This implies that $\delta$ is a constant, whereas $\tilde{\Sigma}$ is a function of one variable

$$\eta = \zeta - \zeta_c(t).$$

At $\zeta > \zeta_c + \delta/2$ we have $\tilde{\Sigma} = \tilde{\Sigma}_0 = \text{const}$. Together with the boundary condition at $\zeta \to \infty$, this gives

$$V(\zeta, t) = 0 \quad \text{at} \quad \zeta > \zeta_c + \delta/2. \tag{32}$$

After passage of the critical layer, at $\zeta < \zeta_c - \delta/2$, the wave does not exist, so $\tilde{\Sigma} = 0$. The solution satisfying the assumption of time-independent breaking process is

$$V(\zeta, t) = V_{max} = \text{const} \quad \text{at} \quad \zeta < \zeta_c - \delta/2, \quad \zeta \gg L(t). \tag{33}$$

Further we observe that the growth rate of the total strength of the current should be equal to the drop of the momentum flux

$$V_{max}\dot{\zeta}_c = \tilde{\Sigma}_0 = \beta \Sigma_0, \tag{34}$$

and, thus,

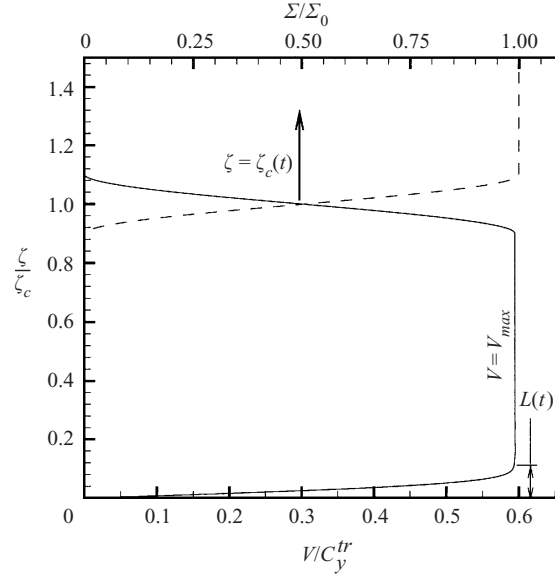$$\dot{\zeta}_c = \text{const}. \tag{35}$$

FIGURE 3. Typical solution of the model problem (20), (30).

The solution is illustrated in figure 3. The wave breaking layer moves from the wall with a constant speed $\dot{\zeta}_c$, leaving behind the mean current with the constant bulk velocity $V_{max}$. The constants can be defined if one knows the details of the process. In particular, both $V_{max} < C_y^{tr}$ (shown in figure 3) and $V_{max} > C_y^{tr}$ are possible. The former corresponds to the 'sub-critical' case $\tau < 1$ when the wave breaks down where mean current velocity substantially smaller than the trace speed. On the other hand, one can imagine the situation where the current velocity is close to $C_y^{tr}$ at $\zeta = \zeta_c$ so that the injection of momentum into the current in the lower part of the wave breaking zone $\zeta < \zeta_c$ can lead to $V_{max} > C_y^{tr}$.

The identity (34) allows us to express both important characteristics of the mean current in a simple form:

$$V_{max} = \tau C_y^{tr}, \quad \dot{\zeta}_c = \frac{\beta}{\tau} \frac{\Sigma_0}{C_y^{tr}}. \tag{36}$$

If we re-scale (36) using $C_y^{tr}$ as the scale for velocity and $\dot{\zeta}_c$, and assume $\tau$ and $\beta$ to be given constants we obtain a self-similar solution depending on one non-dimensional parameter:

$$S \equiv \frac{\Sigma_0}{(C_y^{tr})^2} = Ri^{-1} f(\theta, \alpha, \gamma), \tag{37}$$

where

$$f = 2\pi^2 \frac{\sin^3 \gamma \sin \theta (\cos \gamma \sin \theta \sin \alpha + \cos \theta \cos \alpha)}{(\sin^2 \theta - \cos^2 \theta \cos \gamma)^2}. \tag{38}$$

The same conclusion can be obtained if one considers the original system (20), (30) and rescales the variables using $C_y^{tr}$ as the velocity scale, $v(C_y^{tr})^{-1}$ as the length scale, and $v(C_y^{tr})^{-2}$ as the time scale.

At given values of $\tau$ and $\beta$, the parameter $S$ evaluates the non-dimensional speed of the growth of the current $\dot{\zeta}_c$, which is the main factor determining the current's viability in the real ocean flows. If, further, we fix the Richardson number, the
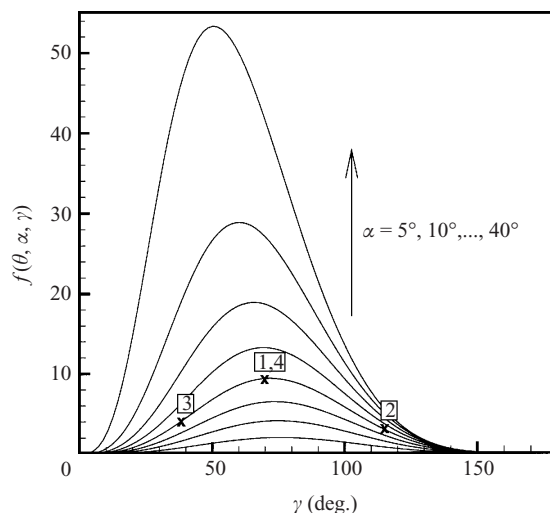
FIGURE 4. Non-dimensional parameter (38) shown as a function of the oblique angle $\gamma$ at different slope angles $\alpha$ and $\theta = \pi/2 - \alpha$. Points labelled 1 to 4 correspond to the values of $\alpha$ and $\gamma$ used in the numerical experiments.

potential of an oncoming wave to create along-slope current is expressed solely by (38). Figure 4 shows $f$ as a function of the oblique angle $\gamma$ at different values of the slope angle $\alpha$ and $\theta = \pi/2 - \alpha$. The strongest mean currents are created by the wave with oblique angle in the range between 40° and 80°. No currents can be produced by almost normal waves with $\gamma \to 0$ or $\gamma \to \pi$.

Another feature of the curves in figure 4 is the growth of $f$ with the slope angle $\alpha$. This suggests that along-slope mean currents are more probable near the steeper slopes typical of islands and seamounts than in the regions where the waves interact with gently sloping oceanic shelves.

## 4. Numerical experiments

### 4.1. *Procedure and parameters*

Several numerical experiments are presented in this section. Their most important parameters are given in tables 1 and 2. The slope angle $\alpha$ is 20° and the wave inclination angle $\theta$ is 70° in all the experiments so that the case of critical reflection is invariably considered.

Each experiment lasts many wave periods $T = 2\pi/\omega$ and consists of two principal phases. During the first phase, which starts at $t = 0$ and ends at some $t_0$ between $10T$ and $20T$, the mean along-slope velocity $\langle v \rangle$ is subtracted from the velocity field $\boldsymbol{u}$ after each time step. The purpose of this becomes clear if we recall the mechanisms of the current generation through the transient effects and spatial viscous decay of the wave discussed in § 3.2. We deliberately exclude these premature currents from consideration because they may not have any counterparts in the real ocean flows of interest, while contaminating the results of the experiments.

Several periods $T$ after the start of the calculations, the wave reaches the bottom and wave breaking starts, which is very similar to that described by Slinn & Riley (1998a, 2001) for normally incident waves. This flow is calculated for several more periods, with the purpose being to achieve a balance between the forcing and near-wall

| Case | $\gamma$ [°] | $C$ | $L_\xi \times L_y \times L_\zeta$ | $N_\xi \times N_y \times N_\zeta$ | $k$ | $-C_{g\zeta}$ | $C_y^{tr}$ | $t_0/T$ | $t_{end}/T$ |
|---|---|---|---|---|---|---|---|---|---|
| 1 | 71.6 | $5.2 \times 10^{-3}$ | $2 \times 2.6074 \times 10$ | $64 \times 64 \times 300$ | 7.43 | $-0.054$ | 0.142 | 17.4 | 56.0 |
| 2 | 114.8 | $5.2 \times 10^{-3}$ | $5 \times 3.003 \times 10$ | $128 \times 64 \times 300$ | 6.74 | $-0.026$ | 0.164 | 38.4 | 68.9 |
| 3 | 37.9 | $5.2 \times 10^{-3}$ | $1.375 \times 3.7648 \times 10$ | $64 \times 128 \times 300$ | 7.95 | $-0.068$ | 0.205 | 10.2 | 24.4 |
| 4 | 71.6 | $3.7 \times 10^{-3}$ | $2 \times 2.6074 \times 10$ | $64 \times 64 \times 300$ | 7.43 | $-0.054$ | 0.142 | 12.0 | 55.4 |

TABLE 1. Specification of the numerical experiments: oblique angles $\gamma$, forcing amplitude $C$, dimensions of the computational domain, numerical resolution, wavenumber $k$, $\zeta$-component of the group velocity $C_{g\zeta}$, $y$-component of the trace speed $C_y^{tr}$, starting point of the mean current generation $t_0/T$ ($T$ is the wave period), total duration of the run $t_{end}/T$.

| Case | $A(\zeta_0, t_0)$ | $A(0.5, t_0)$ | $Re$ | $Ri$ | $\dfrac{\Sigma(\zeta_0, t_0)}{(C_y^{tr})^2}$ | $\dfrac{\Sigma(0.5, t_0)}{(C_y^{tr})^2}$ | $\dfrac{V_{max}^*}{C_y^{tr}}$ | $M$ | $H$ |
|---|---|---|---|---|---|---|---|---|---|
| 1 | $4.7 \times 10^{-2}$ | $3.9 \times 10^{-2}$ | 1410 | 453 | $2.0 \times 10^{-2}$ | $1.4 \times 10^{-2}$ | 0.48 | $0.37 \pm 0.03$ | $0.53 \pm 0.06$ |
| 2 | $5.0 \times 10^{-2}$ | $3.7 \times 10^{-2}$ | 1500 | 400 | $7.4 \times 10^{-3}$ | $4.0 \times 10^{-3}$ | 0.22 | $0.42 \pm 0.02$ | $0.52 \pm 0.01$ |
| 3 | $5.5 \times 10^{-2}$ | $4.7 \times 10^{-2}$ | 1650 | 331 | $1.2 \times 10^{-2}$ | $8.6 \times 10^{-3}$ | 0.70 | $0.35 \pm 0.04$ | $0.56 \pm 0.08$ |
| 4 | $3.3 \times 10^{-2}$ | $2.8 \times 10^{-2}$ | 990 | 918 | $1.0 \times 10^{-2}$ | $7.3 \times 10^{-3}$ | 0.43 | $0.34 \pm 0.03$ | $0.56 \pm 0.04$ |

TABLE 2. Specification of the numerical experiments: maximum wave amplitude $A(\zeta_0, t_0)$, wave amplitude $A(0.5, t_0)$ at $\zeta = 0.5$ and $t = t_0$, actual Reynolds and Richardson numbers calculated using $A(\zeta_0, t_0)$ as the velocity scale, maximum values of normalized momentum flux (parameter $S$ of the model) at $\zeta = \zeta_0$ and $t = t_0$, normalized momentum flux at $\zeta = 0.5$ and $t = t_0$, time-averaged normalized maximum velocity of mean along-slope current $V_{max}^*/C_y^{tr}$, mixing efficiency (41), heat gain coefficient (42). The integration limits for $V_{max}^*$, $M$, and $H$ are $[t_0+6T, t_0+21T]$, $[t_0+4T, t_0+22T]$, $[t_0+10T, t_0+35T]$, and $[t_0+4T, t_0+42T]$ for Cases 1, 2, 3, and 4, respectively.

dissipation. At the end of the first phase of the experiment, at $t = t_0$, the incident wave train has a statistically steady distribution in the whole computational domain. An illustration is given in figures 2($b, c$), where the total wave energy and the momentum flux averaged in the ($\xi, y$)-plane are shown as functions of $\zeta$. Remarkably, the results of the calculations are in excellent agreement with the decay law (28). This can be considered as a verification of the closeness of the numerically generated wave to the monochromatic solution (19).

In the course of the second phase of each experiment, starting at $t = t_0$, limitless generation of the mean along-slope current is allowed in the lower part of the computational domain, for, approximately, $\zeta < 0.4 L_\zeta$. We examine the flow in this part only, the upper part serving exclusively for the generation of oncoming wave packets. Note that no large waste of computational resources is associated with such a partition because the grid points are clustered at small $\zeta$.

### 4.2. *Example of current generation*

In this section we give a detailed description to the process of mean current generation due to the breaking of an obliquely incident wave. The description is based on the results of one numerical experiment denoted as Case 1 in tables 1 and 2. The experiment is typical in the sense that the principal features of the flow found in this run are repeatedly reproduced, apart from quantitative variations, in all other experiments.

The evolution of the spatial structure of the flow is illustrated in figure 5. Vertical cross-sections at $y = L_y/2$ are shown including contours of total density (7) ($a$–$c$),
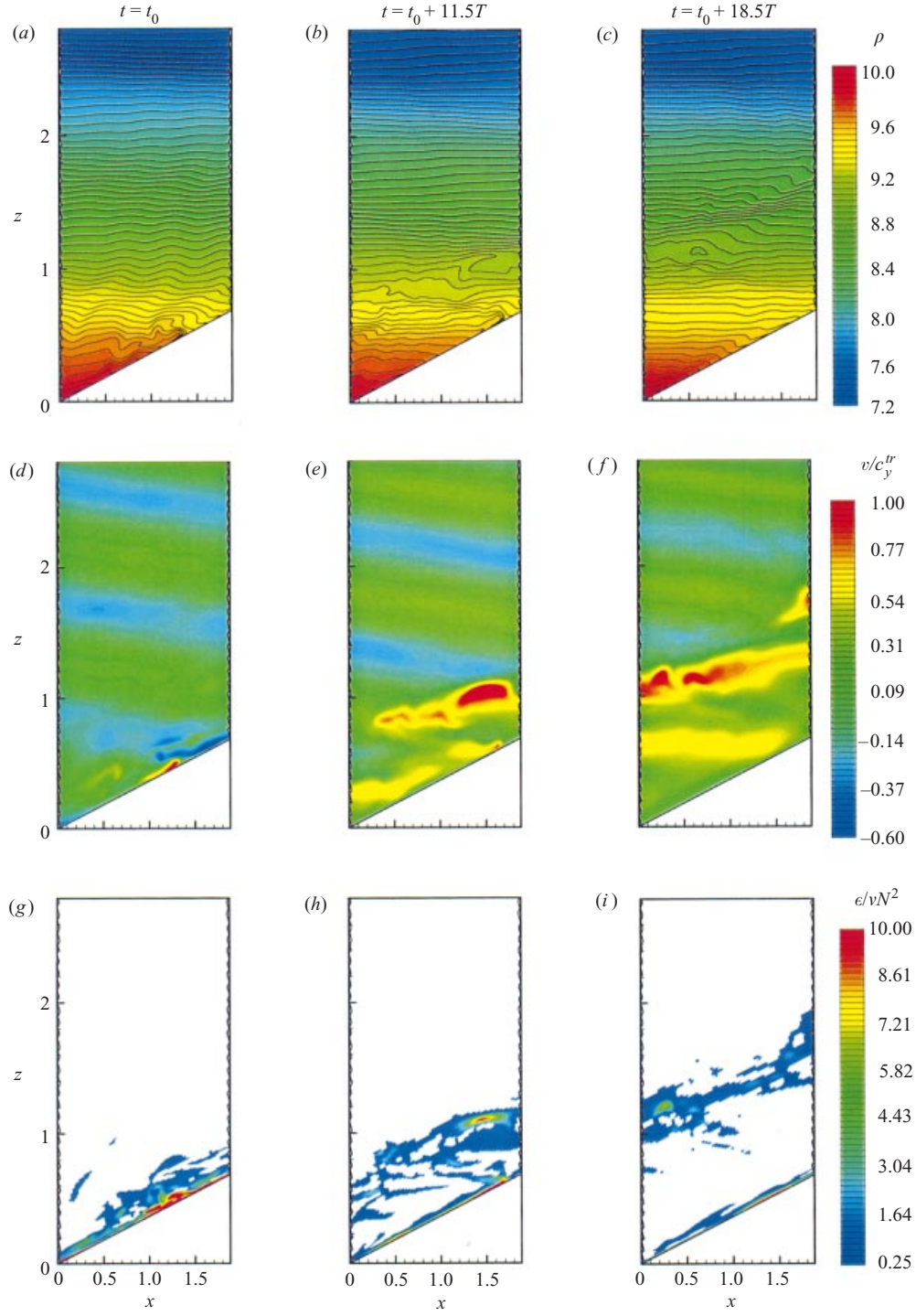
*O. Zikanov and D. N. Slinn*



FIGURE 5. Along-slope current generation in Case 1. Isopycnals (*a–c*), *v*-velocity contours (*d–f*), and kinetic energy dissipation rates $\epsilon/\nu N^2$ (*g–i*) are shown in the vertical cross-section $y_0 = L_y/2$ at $t = t_0$, $t = t_0 + 11.5T$, $t = t_0 + 18.5T$. The contours of energy dissipation rate are blanked at $\epsilon/\nu N^2 < 0.25$.
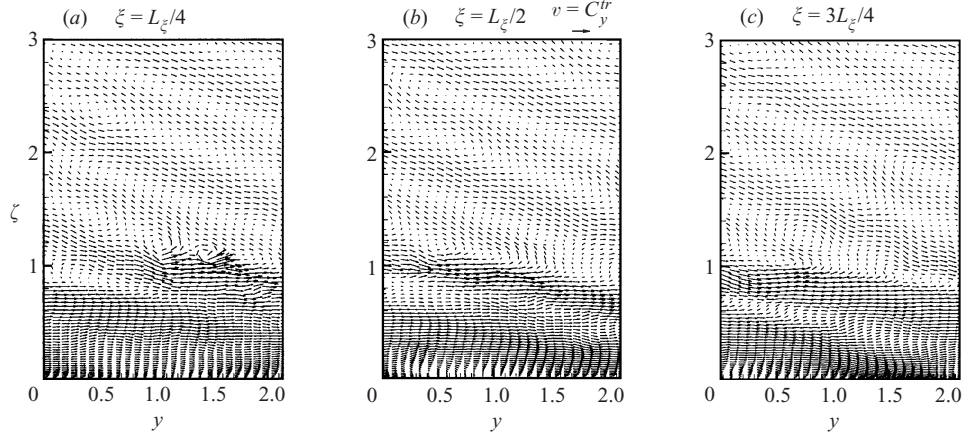
FIGURE 6. Velocity fields calculated in Case 1 at $t = t_0 + 18.5T$. Projections on the $(y, \zeta)$-plane are shown at the cross-sections $\xi = L_\xi/4$, $\xi = L_\xi/2$, and $\xi = 3L_\xi/4$. Every second vector in the $y$- and $\zeta$-directions is plotted. Reference vector $v = C_y^{tr}$ is shown in (*b*).

along-slope velocity component $v$ (*d*–*f*), and viscous dissipation rate $\epsilon$ (*g*–*i*). The direction of wave propagation (group velocity) is downward, to the right, and into the page in this experiment.

Figures 5(*a*), 5(*d*), and 5(*g*) in the left-hand column show the flow at $t = t_0$, i.e. the flow calculated with the mean along-slope current artificially removed. It can be seen that the wave breakdown occurs in a similar fashion to the simulations with normally incident waves (Slinn & Riley 1998*a*, 2001). The wave breaks at the bottom slope and creates a turbulent boundary layer. The outstanding characteristic of this flow, found by Slinn & Riley to be typical for critical reflection at shallow slopes with $\alpha \leqslant 20°$, is a density front moving up-slope. The front speed is equal to the up-slope component of the phase velocity so that the front location always corresponds to a certain phase of the oncoming wave. An important distinction in the oblique case from the cases with normal incidence is that the density front is now accompanied by a strong localized along-slope current (the bright red spot on figure 5*d*).

The plots in the middle and right-hand columns of figure 5 show the flow evolution during the second phase of the experiment, i.e. when the mean along-slope current is allowed to exist. The plots clearly demonstrate that the scenario described in §3.3 is, indeed, realised in the simulations. A strong along-slope current develops near the bottom and expands with time (see figures 5*e* and 5*f*). The maximum velocity of this current slightly exceeds the along-slope trace speed $C_y^{tr}$. However, unlike the simplified theoretical model, the velocity is not constant across the current. A maximum is achieved at the upper boundary, the flow below being considerably slower, with velocity ranging between 0.1 and 0.7 of the trace speed. It can be seen in figures 5(*e*, *f*) that the current is subject to wave-like inhomogeneity, obviously the result of penetration of the oncoming wave.

Further information on the spatial structure of the flow can be found in figures 6 and 7 where two-dimensional projections of the velocity field on different cross-sections of the domain are shown. In particular, it can be seen that the along-slope current occupies the whole domain in the $\xi$- and $y$-directions.

The plots of along-slope velocity in figures 5(*e*, *f*) and 6 demonstrate the presence of a well-defined critical layer, which is approximately parallel to the bottom slope
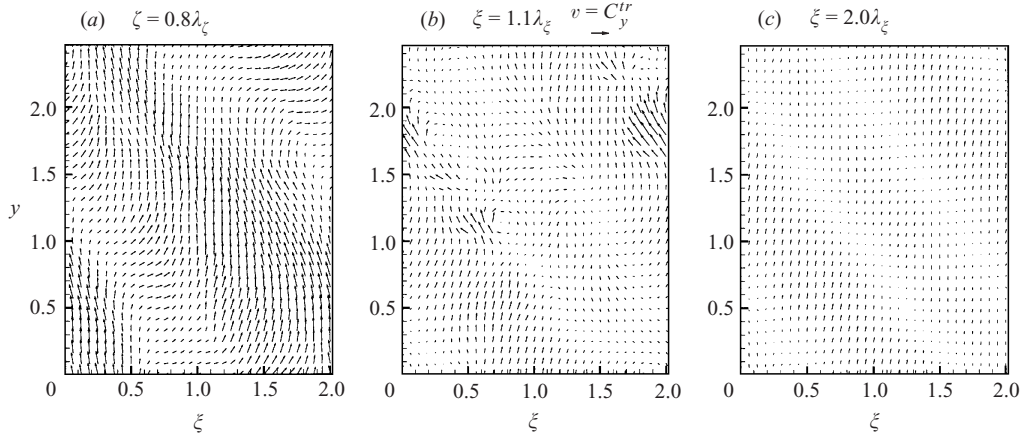
FIGURE 7. Velocity fields calculated in Case 1 at $t = t_0 + 18.5T$. Projections on the $(\xi, y)$-plane are shown at the cross-sections $\zeta = 0.8\lambda_\zeta$, $\zeta = 1.1\lambda_\zeta$, and $\zeta = 2.0\lambda_\zeta$. Every second vector in the $\xi$- and $y$-directions is plotted. Reference vector $v = C_y^{tr}$ is shown in (*b*).
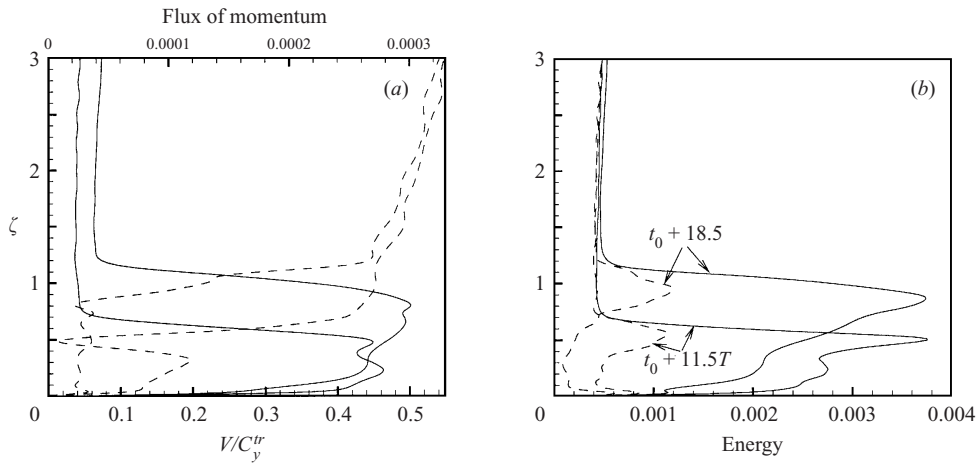


FIGURE 8. Along-slope current generation in Case 1. Calculated flow properties are averaged in the $\xi$- and $y$-directions and shown as functions of $\zeta$ at $t = t_0 + 11.5T$ and $t = t_0 + 18.5T$. (*a*) Mean along-slope velocity $V(\zeta, t)$ (solid lines) and the flux of momentum $\Sigma(\zeta, t)$ (dashed lines). (*b*) kinetic energy $KE(\zeta, t)$ (solid lines) and potential energy $PE(\zeta, t)$ (dashed lines).

and located at the upper boundary of the along-slope current. Wave breaking occurs at this layer. It can be seen in the dissipation plots in figures 5(*h*) and 4(*i*) that the zone of turbulent motion, in which the intensive dissipation is characteristic, moves together with the critical layer. As the density plots in figures 5(*b*) and 5(*c*) show, intensive mixing occurs at the critical layer. Below this layer, vertical stratification is re-established.

To analyse the evolution of the mean current we calculated the flow quantities averaged in the plane parallel to the slope. Particular attention was given to the mean along-slope velocity $V(\zeta, t)$, normal flux of momentum $\Sigma(\zeta, t)$, and the kinetic and potential energies $KE(\zeta, t)$, $PE(\zeta, t)$.

Typical snapshots are shown in figure 8. It can be seen that the mean velocity profiles are qualitatively similar to the model profile in figure 3. They consist of a viscous

boundary layer at the bottom, the layer at the top where the current is generated, and the region of approximately constant bulk velocity between them. Note that the flux of momentum decreases to nearly zero through the current generation region.

A note is in order regarding the averaged velocity $V$ in the current. It can be seen in figure 8(a) that it does not exceed $0.5C_y^{tr}$ even if, as demonstrated in figure 5(e, f), maximum along-slope velocity is about $C_y^{tr}$. The reason is the wave penetration into the current that creates zones of reduced velocity as well as other zones of enhanced velocity where wave penetration adds constructively. Since the wave breaking is the only source of along-slope momentum in the flow, we may assume that the mean velocity should remain considerably smaller than $C_y^{tr}$ at later stages of current evolution when the current grows broad in comparison to $\lambda_\zeta$ and all the wave-like inhomogeneities are smoothed by dissipation.

One more peculiarity of the mean current profiles obtained in the simulations is that $V(\zeta, t) > 0$ even far above the critical layer (see figure 8a). This is, obviously, due to the divergence of the flux of momentum caused by the viscous decay of the incident wave (see § 3.2). The viscously generated current was found to have only a weak influence on the properties of the wave propagating through it as long as the current velocity was considerably smaller than $C_y^{tr}$. In each numerical experiment, the calculations were stopped when this velocity became comparable to $C_y^{tr}$ at some point and a second critical layer developed.

Figure 8(b) shows the dramatic impact of the wave breakdown at the critical layer interface and mean current generation on the vertical energy distribution. In the oncoming wave, $KE(\zeta, t)$ and $PE(\zeta, t)$ are virtually equipartitioned. This is one more confirmation of the closeness of our numerically generated wave to the monochromatic solution. The region around the critical layer is characterized by the drastic increase of both the potential and kinetic energy, indicative of intensive turbulent mixing created by wave breakdown. Below the critical layer, where the vertical stratification is essentially restored, the potential energy decreases. The kinetic energy density is now dominated by the energy of the mean current and remains considerably larger than in the incident wave.

The profiles shown in figure 8 may be used to estimate the mean thickness of the turbulent layer in which wave breaking and current generation occur. The layer can be defined as the region where the velocity and kinetic energy of the mean current grow from the viscously generated values to the maximum values. The thickness of this layer varied considerably in the numerical experiments. Depending on wave parameters and time, values between $0.5\lambda_\zeta$ and $\lambda_\zeta$ were found.

Another way to describe the geometry of the wave breaking zone is to estimate the thickness and location of the turbulent mixing layer characterized by increased potential energy density $PE(\zeta, t)$. In the calculations, the mixing layer is typically larger (thickness between $0.7\lambda_\zeta$ and $1.1\lambda_\zeta$) than the turbulent layer defined through the increase in kinetic energy. As illustrated in figure 8(b), large-amplitude density perturbations associated with increased potential energy penetrate substantially into the mean current or persist from earlier wave breaking events.

Figure 9(a) shows the terms of the total energy balance equation, which is the sum of (17) and (18). Several important conclusions can be drawn concerning the validity of the simulations. First, the work input by the wave forcing, $W$, is statistically steady with very weak oscillations. Further, the energy flux through the upper boundary of the computational domain, $S_f$, is negligibly small in the calculations. Very important also is that the rate of dissipation in the resolved scales, $\epsilon + \chi$, remains much larger than the rate of dissipation by the subgrid-scale filter, $F$. Therefore, the filter accounts
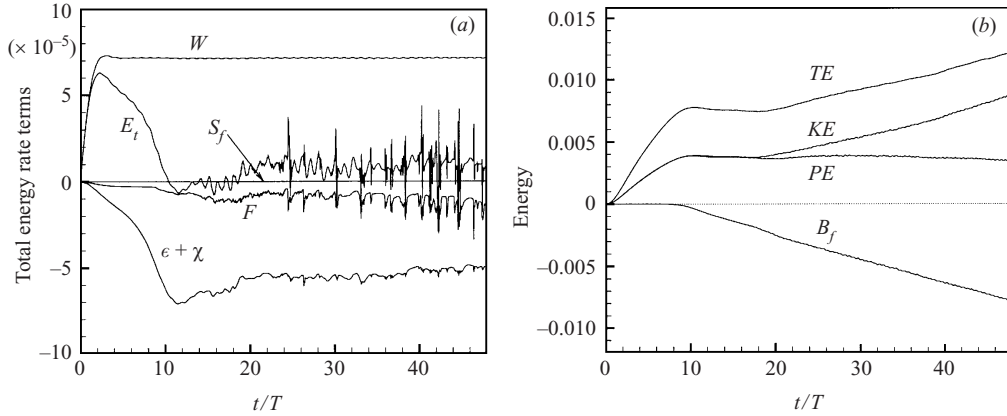
FIGURE 9. Calculations in Case 1. (*a*) Evolution of terms in total energy equation (17)+(18): work input $W$, time derivative of the energy $E_t$, dissipation and diffusion rates in the resolved scales $\epsilon + \chi$ and due to the filter $F$, flux of energy into sponge layer $S_f$. (*b*) Volume integrals of kinetic ($KE$), potential ($PE$), and total ($TE$) energy and the buoyancy flux ($B_f$).

for a small part of the total dissipation and can be considered to have only a slight influence on the dynamics of large scales of the flow.

Figure 9(*b*) shows how the partition of the volume-integrated flow energy changes with time. The buoyancy flux, $B_f$, departs from zero when the leading edge of the wave reaches the bottom and continually grows in amplitude afterwards, indicating a net transfer of wave potential energy to kinetic energy. Similar behaviour was observed in the simulations of normally incident waves by Slinn & Riley (2001). The new feature of our energy plot is the disparity between the kinetic and potential energies starting exactly at the moment $t = t_0 = 17.4T$ when the mean along-slope current is allowed to exist. The excess kinetic energy represents the energy of the along-slope current.

### 4.3. *Effect of wave parameters*

Several numerical experiments were performed to investigate how the process of along-slope current generation changes depending on the parameters of the oncoming wave. Specifications of the experiments are given in tables 1 and 2. For this first study of the phenomenon we restrict consideration to the bottom slope $\alpha = 20°$. The wave inclination to the horizontal is $\theta = 70°$. The effect of the oblique angle is examined in Cases 1, 2, and 3. The influence of the wave amplitude $A$ can be seen from the comparison between Cases 1 and 4.

A point has to be made regarding the fact that $A$ cannot be defined *a priori* in the calculations. Instead, we define the forcing amplitude $C$ (see (12)). The wave amplitude is estimated in the course of simulations according to

$$A_0 = [2(KE(\zeta_0, t_0) + PE(\zeta_0, t_0))]^{1/2}. \tag{39}$$

Here $KE(\zeta_0, t_0)$ and $PE(\zeta_0, t_0)$ are the $\xi$, $y$-averaged profiles of the kinetic and potential energy computed at $t = t_0$, i.e. at the moment when the second phase of the experiment begins with releasing the constraint on the mean along-slope current in the lower portion of the computational domain. The coordinate $\zeta_0$ is determined as that giving the maximum of $KE(\zeta, t)$ and $PE(\zeta, t)$. In all the experiments, the value $\zeta_0 = 5.752$ was obtained. Thus defined, $A_0$ virtually does not change with time at $t > t_0$ and is the amplitude of the wave immediately after emerging from the forcing
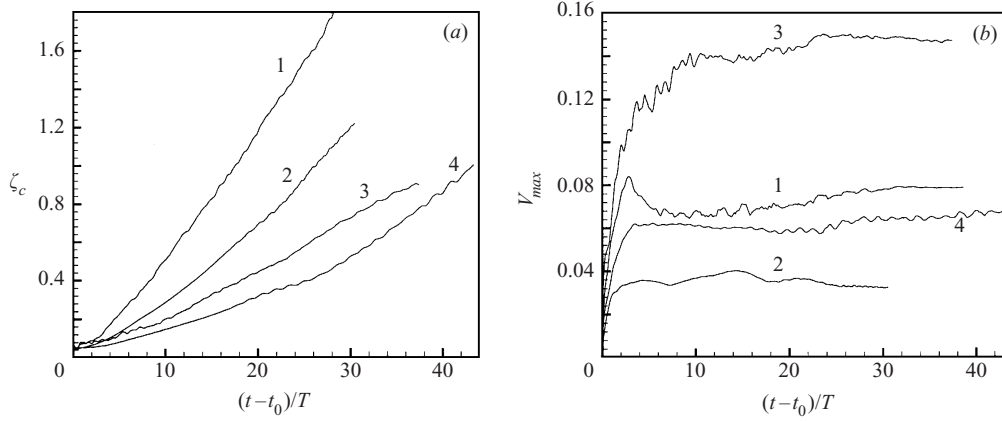
FIGURE 10. Along-slope current generation in numerical experiments 1, 2, 3, and 4: (*a*) distance $\zeta_c(t)$ of the mid-plane of the wave-breaking layer from the bottom; (*b*) maximum velocity $V_{max}$ of the mean current.

region. The actual amplitude of the wave interacting with the critical layer is reduced due to viscous decay. For comparison, table 2 gives the values of $A_0$ and the values of $A(\zeta = 0.5, t_0)$ computed according to (27). A similar procedure is applied to calculate the maximum values $\Sigma(\zeta_0, t_0)$ and $\Sigma(\zeta = 0.5, t_0)$ shown in table 2.

In the course of the experiments, two principal parameters of the mean along-slope current are evaluated: the maximum current velocity $V_{max}$ and the mid-plane of the wave breaking layer $\zeta_c(t)$. For $\zeta_c(t)$ we use the approximation whereby the distance from the wall to the level where the mean current velocity $V(\zeta, t)$ is equal to $V_{max}/2$. The results are summarized in figure 10. It can be seen that the simulations are in agreement with the model of §3.3. After the initial period, where the wave breaks at the bottom, the current generation occurs in a fashion similar to that described by (33) and (35). The maximum velocity remains approximately constant. The deviation of $\zeta_c(t)$ curves from a linear dependence has the obvious explanation that the actual value of the momentum flux $\Sigma(\zeta, t)$ is not a constant but grows with $\zeta$ in the simulations, which implies a growing slope $\dot{\zeta}_c$.

Time-averaged values of $V_{max}$ normalized by the along-slope trace speed $C_y^{tr}$ are given in table 2. The current velocity is considerably smaller than the trace speed, the ratios $V_{max}^*/C_y^{tr}$ ranging between 0.22 and 0.70. Taking into account our definition of the midplane $\zeta_c(t)$ of the turbulent layer, this leads to the estimate $0.2 < \tau < 0.7$ for the parameter $\tau$ used in (30) to formulate the simplified model

The results shown in figure 10 allow us to draw preliminary conclusions concerning the influence of $\gamma$ and $A$ on the along-slope current. Comparing curves 1 and 4 we see that two waves of the same spatial orientation but different amplitude produce mean currents of almost equal maximum velocity (see figure 10*b*). The main effect of the difference in amplitude and, thus, in the flux of momentum $\Sigma$ is on the growth rate of the current zone (slope of the curves $\zeta_c(t)$ in figure 10*a*).

The comparison between Cases 1, 2, and 3 with different oblique angles is complicated by the fact that the actual wave amplitude $A$ is also slightly different in these cases even though the forcing amplitude $C$ is the same. One reason is that the initial amplitudes $A_0$ produced by the forcing (12) are slightly different. Moreover, in accordance with (28), changing wavenumber $k$ and group velocity $C_{g\zeta}$ yield different viscous decay at the same $\zeta$. Nevertheless, some conclusions can be drawn. In
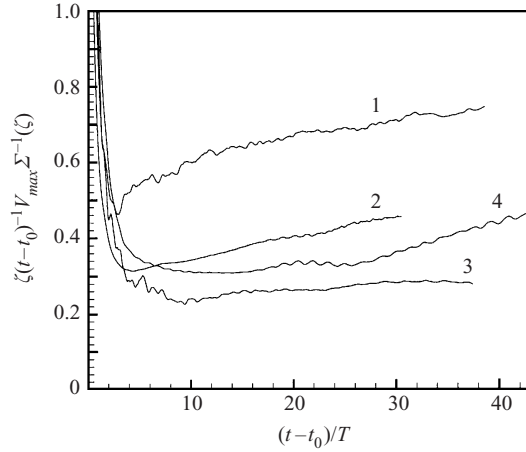
FIGURE 11. Results of the numerical experiments 1 to 4: part of the flux of momentum transferred into the mean current estimated according to (40).

particular, one can see that the waves with smaller oblique angles tend to produce mean currents of larger velocity.

It is pertinent to point out here that even if $\Sigma$ is approximately equal in Cases 1, 2, and 3, the parameter $S = \Sigma/(C_y^{tr})^2$, which defines the current generation according to our simplified model, varies considerably between the cases. The estimated values of $S$ are given in table 2 and its dependence on the oblique angle was discussed in §3.3.

Figure 11 presents an attempt to estimate the unknown coefficient $\beta$ used in this simplified model to account for the portion of the wave flux of momentum injected into the mean current (see (34)). We assume for a moment that (34) holds in the simulations and that the momentum flux $\Sigma$ depends on $\zeta$ as (28), $\Sigma(\zeta_0)$ being the maximum value given in table 2. The speed of the critical layer $\dot{\zeta}_c$ cannot be reliably estimated in the calculations because of violent fluctuations caused by large turbulent eddies in the wave breaking layer. This obstacle is circumvented by assuming that

$$\zeta_c = \dot{\zeta}_c(t - t_0)$$

and substituting $\zeta_c(t - t_0)^{-1}$ for $\dot{\zeta}_c$ in (34). As a result we obtain

$$\beta \approx \zeta_c(t - t_0)^{-1} V_{max}\Sigma^{-1}(\zeta). \tag{40}$$

The coefficient (40) is plotted in figure 11 as a function of time. The time-averaged values of $V_{max}$ given in table 2 are used. One can see that $\beta$ can take, at least, values between 0.2 and 0.8. Its time-dependence, apart from the initial stage of each experiment, is rather weak. On the other hand, a change in the oblique angle or wave amplitude leads to considerable variations of $\beta$.

The last aspect of the computed results to be discussed here is the mixing efficiency of the turbulent flow created due to the wave breaking. Following Slinn & Riley (2001) we define the mixing efficiency as

$$M \equiv \frac{-\int_{t_1}^{t_2} [\bar{\chi} + \overline{F_{PE}}]\mathrm{d}t}{\int_{t_1}^{t_2} [\overline{W_{KE}} + \overline{W_{PE}}]\mathrm{d}t}, \tag{41}$$

which is the portion of the wave energy going to irreversible mixing of the density

field. The time integration in (41) is over the period $[t_1, t_2]$ of the flow evolution, where the initial transient processes are finished and a well-established critical layer moves upwards. In the same manner, we define the heat gain coefficient

$$H \equiv \frac{-\int_{t_1}^{t_2} [\bar{\epsilon} + \overline{F_{KE}}] \mathrm{d}t}{\int_{t_1}^{t_2} [\overline{W_{KE}} + \overline{W_{PE}}] \mathrm{d}t}, \tag{42}$$

which gives the portion of energy dissipated as heat. There is also a small portion of energy which is radiated by reflected waves or induced mean currents. The values of $M$ and $H$ are given in table 2 together with the tolerance limits.

In the simulation of bottom turbulent layers produced by breaking normally incident waves, Slinn & Riley (2001) found that the ratios (41) and (42) quickly achieve statistically steady values which do not change with further increase of $t_2$. Typically, the values were about 0.35 for $M$ and 0.55 for $H$. Examining the data in table 2 shows that the mixing efficiency and heat gain are approximately the same. However, a weak continual change with $t_2$ was detected in all the experiments. Among other reasons, this can be related to the change of the amplitude of the oncoming wave at the critical layer, which occurs as the critical layer moves upwards.

## 5. Possibility of current generation in the ocean

The numerical simulations discussed in this paper are performed at Reynolds numbers which are many orders of magnitude smaller than the Reynolds number of internal waves in the ocean. Moreover, we consider the case of a relatively steep slope $\alpha = 20°$, whereas typical values on the oceanic shelf are between 2° and 5°. The reasons for these inconsistencies are related to the present computational limitations of numerical simulations. Both an increase in the Reynolds number and decrease in the slope would require unacceptable growth of the number of grid nodes (in all three dimensions in the former case and in the $\xi$-direction in the latter).

Nevertheless, we can use the model predictions obtained in §3.3 and confirmed by the numerical experiments to consider how the mechanism of along-slope current generation described in this paper could apply in more realistic ocean flows. From the whole spectrum of internal waves existing in the ocean we shall choose just one monochromatic wave having the critical inclination angle to the horizontal and estimate the along-slope current that can be generated by the breakdown of this wave. It should be emphasized that the wave is assumed to persist for long time, sufficient for the thickness of the mean current to become about a wavelength or larger so that the current can withstand the impact of oncoming waves.

As an example, we consider a wave with the moderate wavelength $\lambda = 10^3$ m and the amplitude (maximum velocity) $A = 0.2 \,\mathrm{m\,s^{-1}}$. The buoyancy frequency is $N = 2 \times 10^{-3} \mathrm{s}^{-1}$ and the oblique angle is $\gamma = 71.6°$. Formulas (23) and (29) are used to calculate the radiation stress $\Sigma_0$ and the trace speed $C_y^{tr}$.

Table 3 shows the results for the slopes $\alpha = 2°$, 5°, and 20°. The angle of wave propagation to the horizontal is critical, $\theta = 90° - \alpha$. The values of the parameter $S$ are of the same order of magnitude as in our computations (cf. table 2). This suggests that the generation of along-slope currents in the ocean may occur in a manner similar to that observed in the numerical simulations.

Based on the averaged values of $V_{max}/C_y^{tr}$ in table 2 it is reasonable to assume

| $\alpha$ (deg.) | $\Sigma_0$ [m² s⁻²] | $C_y^{tr}$ [m s⁻¹] | $S$ | $V_{max}$ [m s⁻¹] | $\dot{\zeta}_c$ [m s⁻¹] | $T$ [s] | $T\dot{\zeta}_c$ [m] |
|---|---|---|---|---|---|---|---|
| 2 | $8.70 \times 10^{-4}$ | 0.335 | $7.73 \times 10^{-3}$ | 0.168 | $5.19 \times 10^{-3}$ | $9.0 \times 10^4$ | 233 |
| 5 | $2.16 \times 10^{-3}$ | 0.335 | $1.92 \times 10^{-2}$ | 0.168 | $1.29 \times 10^{-2}$ | $3.6 \times 10^4$ | 232 |
| 20 | $7.54 \times 10^{-3}$ | 0.335 | $6.70 \times 10^{-2}$ | 0.168 | $4.50 \times 10^{-2}$ | $9.2 \times 10^3$ | 206 |

TABLE 3. Model estimates for a sample oceanic internal wave propagating at oblique angle $\gamma = 71.6°$: slope $\alpha$, flux of along-slope momentum $\Sigma_0$, along-slope trace speed $C_y^{tr}$, model parameter $S$, inferred velocity of the mean current $V_{max} = C_y^{tr}/2$, corresponding speed of critical layer $\dot{\zeta}_c$, wave period $T$, distance covered by critical layer during one wave period.

that, in the ocean, the velocity of the mean current is about $0.5C_y^{tr}$. This allows us to estimate the speed of the critical layer $\dot{\zeta}_c$ as the ratio of $\Sigma_0$ to $V_{max}$. The data in table 3 show rapid expansion of the mean current. At all three values of the slope angle $\alpha$, the current zone covers the wavelength $\lambda$ in several wave periods $T$.

It is interesting to note that, at given wavelength and oblique angle, the trace speed $C_y^{tr}$ and, thus, the current velocity $V_{max}$ do not depend on the angle $\theta$ of wave propagation. Moreover, according to the expressions for the wave period $T = 2\pi/N\cos\theta$ and the momentum flux (22), the dominant term in the product $T\dot{\zeta}_c$ is proportional to $\cos^2\alpha$ at small $\alpha$. The result is in table 3. The distance covered by the critical layer during one wave period depends only slightly on the slope angle $\alpha$.

To summarize, if isolated wave packets with a dominant frequency and directionality arrive at a sloping boundary the approximate dynamics we have explored here might be produced. The critical reflection of internal waves on shallow slopes could generate intensive broad along-slope currents in the ocean.

## 6. Discussion and concluding remarks

The numerical experiments presented in this paper demonstrate that obliquely incident internal waves breaking at a bottom slope may generate a flow which is significantly different from that obtained previously in the case of normal incidence. The reason for this is the flux of unbalanced along-slope momentum associated with the incident wave. As the wave breaks, the momentum accumulated in the boundary region gives rise to an along-slope current. As soon as the mean along-slope velocity approaches the wave trace speed in the same direction, wave breaking occurs at the external boundary of the current, being the result of a critical layer interaction. This leads to the expansion of the current zone and outward drift of the wave breaking layer. In an idealized case of a steady monochromatic wave in a semi-infinite domain from a source at infinity one would expect an infinitely expanding current.

The numerical results are in agreement with a simple theoretical model based on the law of conservation of momentum and the concept of radiation stress. In particular, the experiments support the model's conclusions that the critical layer moves with a constant speed and that the mean velocity of the along-slope current does not change with distance from the bottom outside the viscous boundary layer.

The mechanism of along-slope current generation is, certainly, only one of many possible mechanisms associated with the propagation and interaction of internal waves. Keeping in mind the complexity of the problem, in this paper we focused on just one aspect. Such important questions as the Earth's rotation, wave–wave interaction near the critical layer and interaction between the mean current and other
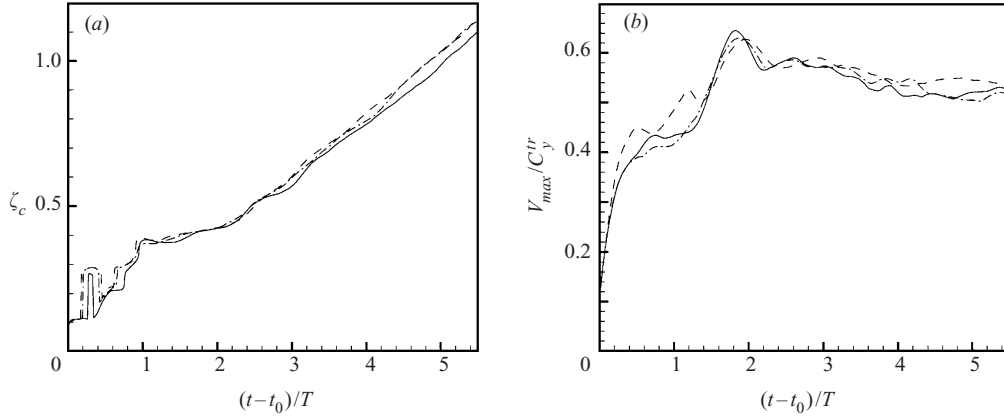
FIGURE 12. Calculations with $\gamma = 72.6°$, $C = 5.2 \times 10^{-3}$, and $L_\zeta = 6\lambda_\zeta$: ———, $L_\xi = \lambda_\xi$ and $L_y = \lambda_y$; — — —, $L_\xi = 2\lambda_\xi$ and $L_y = \lambda_y$; — · — · —, $L_\xi = \lambda_\xi$ and $L_y = 2\lambda_y$; (*a*) distance $\zeta_c(t)$ of the mid-plane of the wave-breaking layer from the bottom; (*b*) maximum velocity $V_{max}$ of the mean current.

waves besides the one causing the current generation are planned for future studies. The ultimate goal should be the understanding of the realistic situation where multiple wave packets corresponding to the whole Garrett–Munk spectrum of oceanic internal waves (Garrett & Munk 1979) are present. One important feature of this situation may be that the mean current $V(\zeta, t)$ initially created by a wave or waves propagating at the critical angle $\theta$ can then receive energy from all other waves satisfying the critical level condition at some $\zeta$.

## 7. Appendix: Accuracy of numerical presentation

In numerical simulations of flows like that considered in the paper, the question of accuracy of the numerical experiments arises at both ends of the length scale spectrum. The motions on small, dissipative scales have to be resolved or accounted for by a relevant subgrid-scale model. On the other hand, in the situation when the flow is driven by large-scale turbulent eddies and the computational domain presents only a part of the real flow domain, the right choice of the size of computational domain becomes important. In our case this especially concerns the dimensions $L_\xi$ and $L_y$ parallel to the bottom slope.

The presentation of small-scale motions has already been discussed in §4.2 where the terms of the energy balance equation were calculated (see figure 9*a*). The rate of dissipation and diffusion in the numerically resolved scales, $\epsilon + \chi$, was found to be much larger than the rate of dissipation and diffusion $F$ produced by the subgrid-scale filter. Therefore, at the Reynolds number used in the numerical experiments, a specific type of subgrid-scale model may affect only slightly the dynamics of large scales.

In all our simulations, the horizontal dimensions $L_\xi$ and $L_y$ were taken equal to the wavelengths of the oncoming wave, $\lambda_\xi$ and $\lambda_y$. This is a potentially dangerous choice since, as soon as the largest turbulent eddy in the breaking layer becomes comparable

in size to $\lambda_\xi$ or $\lambda_y$, the periodic boundary conditions impose a distorting effect on the flow.

In order to check the influence of $L_\xi$ and $L_y$ we performed three additional experiments, the results of which are illustrated in figure 12. The oblique angle $\gamma$ and the forcing amplitude $C$ were the same as in Case 1 of the main series of simulations. A smaller computational domain with $L_\zeta = 6\lambda_\zeta$ was used, so that the vertical resolution could be reduced to $N_\zeta = 200$. Different combinations of the horizontal dimensions were tried: $L_\xi = \lambda_\xi$ and $L_y = \lambda_y$, $L_\xi = 2\lambda_\xi$ and $L_y = \lambda_y$, $L_\xi = \lambda_\xi$ and $L_y = 2\lambda_y$. One can see from figure 12 that the values of two flow parameters most important in our study, the coordinate of the midplane of wave breaking layer, $\zeta_c(t)$, and the maximum velocity of the current, $V_{max}$, are very close in all three experiments. The conclusion is that the choice of $L_\xi = \lambda_\xi$ and $L_y = \lambda_y$ does not have a considerable impact on the generation of the mean current.

## REFERENCES

BOOKER, J. R. & BRETHERTON, F. P. 1967 The critical layer for internal gravity waves in a shear flow. *J. Fluid Mech.* **27**, 513–539.

BOWEN, A. J. 1969 The generation of longshore currents on a plane beach. *J. Marine Res.* **27**, 206–215.

BRETHERTON, F. P. 1966 The propagation of groups of gravity internal waves in a shear flow. *Q. J. R. Met. Soc.* **92**, 545–563.

CACCHIONE, D. & WUNSCH, C. 1974 Experimental study of internal waves over a slope. *J. Fluid Mech.* **66**, 223–239.

DE SILVA, I. P. D., IMBERGER, J. & IVEY, G. N. 1997 Localized mixing due to a breaking internal wave ray at a sloping bed. *J. Fluid Mech.* **350**, 1–27.

DUNKERTON, T. J., DELISI, D. P. & LELONG, M.-P. 1998 Alongslope current generation by obliquely incident internal gravity waves. *Geophys Res. Lett.* **25**, 3871–3874.

DURRAN, D. R., BROWN, R., SLINN, D. N. & YANG, M. J. 1993 Towards more accurate wave-permeable boundary conditions *Mon. Weath. Rev.* **121**, 604–620.

ERIKSEN, C. C. 1985 Implication of ocean bottom reflection for internal wave spectra and mixing. *J. Phys. Oceanogr.* **15**, 9, 1145–1156.

ERIKSEN, C. C. 1998 Internal wave reflection and mixing at Fieberling Guyot. *J. Geophys. Res.* **103**, 2977–2994.

GARRETT, C. & MUNK, W. 1979 Internal waves in the ocean. *Ann. Rev. Fluid Mech.* **11**, 339–369.

HOGG, N. G. 1971 Longshore currents generated by obliquely incident internal waves. *Geophys. Fluid Dyn.* **2**, 361–376.

IVEY, G. N. & NOKES, R. I. 1989 Vertical mixing due to the breaking of critical internal waves on sloping boundaries. *J. Fluid Mech.* **204**, 479–500.

KOOP, C. G. 1981 A preliminary investigation of the interaction of internal gravity waves with a steady shearing motion. *J. Fluid Mech.* **113**, 347–386.

KOOP, C. G. & McGEE, B. 1986 Measurements of internal gravity waves in a continuously stratified flow. *J. Fluid Mech.* **172**, 453–480.

LEDWELL, J. R., WATSON, A. J. & LAW, C. S. 1993 Evidence for slow mixing across the pycnocline from an open-ocean tracer-release experiment. *Nature* **364**, 701–703.

LELE, S. K. 1992 Compact finite difference schemes with spectral-like resolution. *J. Comput. Phys.* **103**, 16–42.

LESIEUR, M. 1987 *Turbulence in Fluids: Stochastic and Numerical Modeling*. Nijhoff, Dordrecht.

LONGUET-HIGGINS, M. S. 1970 Longshore currents generated by obliquely incident sea waves; Parts 1, 2. *J. Geophys. Res.* **75**, 6778–6801.

LONGUET-HIGGINS, M. S. & STEWART, R. W. 1964 Radiation stress in water waves; a physical discussion, with applications. *Deep-Sea Res.* **11**, 529–562.

MUNK, W. H. 1966 Abyssal Recipes. *Deep-Sea Res.* **2**, 361–376.

PHILLIPS, O. M. 1977 *The Dynamics of the Upper Ocean*, 2nd edn. Cambridge University Press.

Polzin, K. L., Toole, J. M., Ledwell, R. W. & Schmitt, R. W. 1997 Spatial variability of turbulent mixing in the abyssal ocean. *Science* **276**, 93–96.

Roberts, J. 1975 *Internal Gravity Waves in the Ocean*, Marcel Dekker.

Slinn, D. N. 1995 Numerical simulation of turbulent mixing caused by internal wave reflection from sloping boundaries. PhD thesis, University of Washington.

Slinn, D. N., Allen, J. S. & Holman, R. A. 2000 Alongshore currents over variable beach topography. *J. Geophys. Res.* **105**, 16971–16998.

Slinn, D. N., Allen, J. S., Newberger, P. A. & Holman, R. A. 1998 Nonlinear shear instabilities of alongshore currents over barred beaches. *J. Geophys. Res.* **103**, 18357–18379.

Slinn, D. N. & Riley, J. J. 1996 Turbulent mixing in the oceanic boundary layer caused by internal wave reflection from sloping terrain. *Dyn. Atmos. Oceans* **24**, 51–62.

Slinn, D. N. & Riley, J. J. 1998a Turbulent dynamics of a critically refracting internal gravity wave. *Theor. Comput. Fluid Dyn.* **11**, 287–310.

Slinn, D. N. & Riley, J. J. 1998b A model for the simulation of turbulent boundary layers in an incompressible stratified flow. *J. Comput. Phys.* **144**, 550–602.

Slinn, D. N. & Riley, J. J. 2001 Internal wave reflection from sloping boundaries. Submitted to *J. Fluid Mech.*

Thorpe, S. A. 1981 An experimental study of critical layers. *J. Fluid Mech.* **193**, 321–344.

Thorpe, S. A. 1997 On the interaction of internal waves reflecting from slopes *J. Phys. Oceanogr.* **27**, 2072–2078.

Thorpe, S. A. 1999 The generation of alongslope currents by breaking internal waves. *J. Phys. Oceanogr.* **29**, 29–38.

Winters, K. B. & D'Asaro, E. A. 1994 Three-dimensional wave instability near a critical layer. *J. Fluid Mech.* **272**, 255–284.

Winters, K. B., Lombard, P. N., Riley, J. J. & D'Asaro, E. A. 1995 Available potential energy and mixing in density-stratified fluids. *J. Fluid Mech.* **289**, 115–128.

Winters, K. B. & Riley, J. J. 1992 Instability of internal waves near a critical layer. *Dyn. Atmos. Oceans* **16**, 249–278.

Wunsh, C. 1973 On the mean drift in large lakes. *Limnol. Oceanogr.* **18**, 793–795.